

Roles of Amphipathic Helices and the Bin/Amphiphysin/Rvs (BAR) Domain of Endophilin in Membrane Curvature Generation*

Received for publication, March 26, 2010, and in revised form, April 16, 2010. Published, JBC Papers in Press, April 23, 2010, DOI 10.1074/jbc.M110.127811

Christine C. Jao[†], Balachandra G. Hegde[‡], Jennifer L. Gallop^{§2}, Prabhavati B. Hegde[‡], Harvey T. McMahon[§], Ian S. Haworth[¶], and Ralf Langen^{‡3}

From the [†]Zilkha Neurogenetic Institute, University of Southern California, Los Angeles, California 90033, the [§]Medical Research Council Laboratory of Molecular Biology, Hills Road, Cambridge CB2 0QH, United Kingdom, and the [¶]Department of Pharmacology and Pharmaceutical Sciences, University of Southern California School of Pharmacy, Los Angeles, California 90089

Control of membrane curvature is required in many important cellular processes, including endocytosis and vesicular trafficking. Endophilin is a bin/amphiphysin/rvs (BAR) domain protein that induces vesicle formation by promotion of membrane curvature through membrane binding as a dimer. Using site-directed spin labeling and EPR spectroscopy, we show that the overall BAR domain structure of the rat endophilin A1 dimer determined crystallographically is maintained under predominantly vesiculating conditions. Spin-labeled side chains on the concave surface of the BAR domain do not penetrate into the acyl chain interior, indicating that the BAR domain interacts only peripherally with the surface of a curved bilayer. Using a combination of EPR data and computational refinement, we determined the structure of residues 63–86, a region that is disordered in the crystal structure of rat endophilin A1. Upon membrane binding, residues 63–75 in each subunit of the endophilin dimer form a slightly tilted, amphipathic α -helix that directly interacts with the membrane. In their predominant conformation, these helices are located orthogonal to the long axis of the BAR domain. In this conformation, the amphipathic helices are positioned to act as molecular wedges that induce membrane curvature along the concave surface of the BAR domain.

Biological membranes are subject to constant remodeling, and the control of membrane shape and curvature is essential for many vital cellular functions, such as cell division and motility, endocytosis, and vesicular trafficking (1). Recent work has demonstrated that these processes appear to be governed by proteins that can sense and induce membrane curvature (1, 2), and the molecular mechanisms through which these proteins act have become of interest.

* This work was supported, in whole or in part, by National Institutes of Health Grant GM063915 (to R. L.).

† The on-line version of this article (available at <http://www.jbc.org>) contains supplemental data for simulated annealing molecular dynamics, additional references, Tables S1–S3, and Figs. S1–S5.

‡ Recipient of National Institutes of Health Predoctoral Training Grant T32 GM067587.

² Present address: Dept. of Systems Biology, Harvard Medical School, 200 Longwood Ave., Boston, MA 02115.

³ To whom correspondence should be addressed: Zilkha Neurogenetic Institute, University of Southern California, 1501 San Pablo St., Los Angeles, CA 90033. E-mail: langen@usc.edu.

Epsin and bin/amphiphysin/rvs (BAR)⁴ domain proteins are among the proteins thought to regulate membrane curvature in endocytosis (3–7). *In vitro* experiments show that these proteins can bind to larger vesicles and induce the formation of either small and highly curved vesicles (vesiculation) or narrow and highly curved tubules (3–6, 8). High resolution structural information has been obtained for the aqueous forms of all of these proteins (4–6, 8, 9) and provides a starting point for studying the molecular mechanisms of membrane curvature induction. The crystal structures of the BAR domains of endophilin and amphiphysin have the striking feature that they adopt curved, banana-shaped dimers, as illustrated for the structure of rat endophilin A1 (5) in Fig. 1A. The shapes of these dimers are complementary to that of the curved membranes with which the proteins interact. The concave surfaces of the dimers also have a high density of positively charged residues that are likely to interact favorably with negatively charged membranes, and multiple simultaneous mutations of these residues reduce the membrane interaction (5, 6). These data suggest that the concave surface of the BAR domain plays an important role in membrane curvature generation and that it might act as a rigid, positively charged scaffold (5, 6, 8, 10–16).

It has become clear that additional regions outside the BAR domain also play important roles in membrane curvature induction. These regions are unstructured in solution and are not resolved in crystal structures, but their removal or mutation can abolish or inhibit liposome binding activity and tubulation (5, 6, 8). Using site-directed spin labeling and EPR spectroscopy, we have shown that the endophilin N terminus undergoes a structural reorganization from an unfolded state in solution to an amphipathic helix (helix 0) that inserts into the membrane at the level of the head group (5). The inserted helix is likely to act as a molecular wedge that creates a strain in the outer leaflet and thereby promotes membrane curvature. Endophilin also has a central region (residues ~62 to 86) that is disordered in the crystal structure of the rat protein (5) but partly helical (residues 63 to 70) in the crystal structure of the human protein (8). This region has also been proposed to form a helix that inserts into the membrane (5, 17), but detailed experimental

⁴ The abbreviations used are: BAR, bin/amphiphysin/rvs; NiEDDA, nickel ethylenediamine-*N,N'*-diacetic acid; SAMD, simulated annealing molecular dynamics; DEER, double electron-electron resonance.

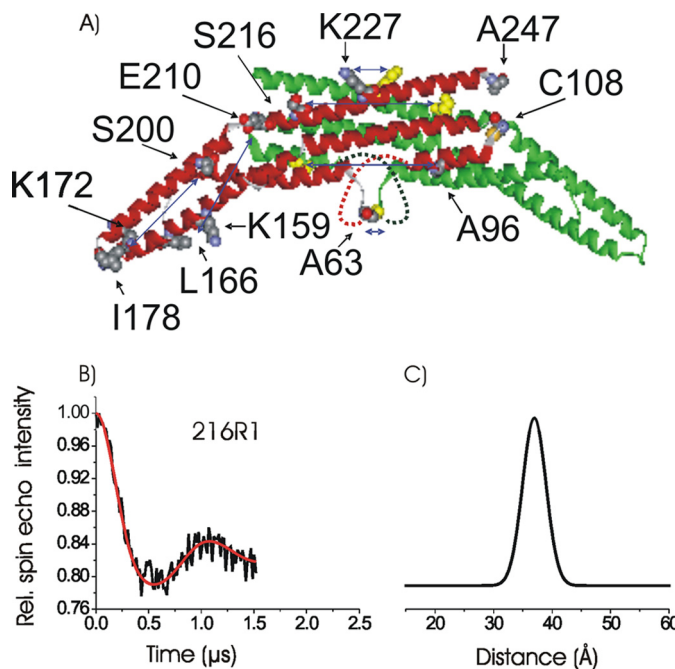


FIGURE 1. Crystal-like dimer structure is retained upon membrane interaction. *A*, crystal structure of rat endophilin A1 (Protein Data Bank code 2C08) indicating the positions of the spin-labeled sites. The individual subunits are shown in green and red, respectively. The disordered insert in helix 1 is not resolved in the crystal structure and is illustrated schematically by the dashed lines. Blue lines with two arrowheads indicate pairs of residues selected for distance measurements. *B*, time evolution data from a four-pulse DEER experiment for the 216R1 derivative in its membrane-bound form. The baseline subtracted data are shown in black, whereas the gaussian fit is shown in red. *C*, distance distribution corresponding to the observed oscillation.

evidence is still lacking. A functional role for this region has recently been supported by genetic rescue experiments in *Drosophila* (18).

Here, we investigated the roles of helix insertion and scaffolding by examining the structure of rat endophilin A1 upon vesiculation. Previous work on annexins showed that curvature-dependent membrane interactions can lead to major conformational reorganization of a protein (19). Thus, our first goal was to test whether the overall structure of the endophilin BAR domain is retained upon membrane interaction and, if so, how its concave surface interacts with the membrane. We then investigated the structure of the central insert (residues 64–86) in the membrane-bound protein using site-directed spin labeling and EPR spectroscopy. The information obtained was then used in a computational refinement to generate three-dimensional atomistic models of membrane-bound endophilin.

EXPERIMENTAL PROCEDURES

Preparation of Spin-labeled Rat Endophilin A1 Derivatives—Single and double cysteine mutants of rat endophilin A1 were expressed and purified as described previously (5). Proteins were reacted with 5× molar excess of the spin label MTSL (1-oxy-2,2,5,5-tetramethyl-d-pyrroline-3-methyl)-methanethiosulfonate, which generates the spin-labeled side chain R1. Unreacted spin label was separated using PD10 columns.

Liposome Preparation—Folch fraction I, type I, was purchased from Sigma-Aldrich. Lipids were dried with nitrogen gas and desiccated overnight. They were resuspended in 20 mM

Hepes, pH 7.4, 150 mM NaCl, treated to brief bath sonication, and extruded through 400-nm pore filters using the Avanti mini-extruder.

Continuous Wave EPR Experiments—2 μM spin-labeled protein was combined with 1.4 mg/ml Folch liposomes and incubated at room temperature for 20 min. After incubation, unbound proteins were separated from membrane-bound proteins by high speed centrifugation at 152,800 × g for 20 min at 22 °C. EPR spectra were then obtained for the membrane-bound portion and also for samples in the absence of liposomes. Spectra were collected using a Bruker EMX spectrometer fitted with a dielectric resonator at 1.59-mW incident microwave power and a scan width of 100 gauss. Power saturation experiments to determine O₂ and NiEDDA accessibility (ΠO₂ and ΠNiEDDA, respectively) have previously been described (20). Accessibility data were obtained using oxygen from air in equilibrium with buffer, and 10 mM NiEDDA. The Φ parameter was calculated by the relationship $\Phi = \ln(\Pi(O_2)/\Pi(NiEDDA))$. The immersion depth was calibrated using 1-palmitoyl-2-stearoyl-(n-DOXYL)-sn-glycero-3-phosphocholine (Avanti Polar Lipids) as described previously (20). We obtained the following relation between immersion depth (*d*) and Φ: $d[\text{Å}] = 6.3*\Phi - 3.9$. This immersion depth represents the depth of the nitroxide moiety.

Pulsed EPR and Distance Analysis—Samples were prepared by combining 4 μM protein and 1.4 mg/ml Folch liposomes. After incubation for 20 min at room temperature, samples were centrifuged at 152,800 × g for 20 min, and the pellet was recovered for measurement. The pellet was resuspended in buffer, and 20–25% sucrose was used as cryoprotectant before loading into quartz capillaries. Samples were flash frozen, and data were acquired at 78 K. Four-pulse double electron-electron resonance (DEER) experiments were performed using a Bruker Elexsys E580 X-band pulse EPR spectrometer fitted with a 3-mm split ring (MS-3) resonator, a continuous flow helium cryostat (CF935; Oxford Instruments), and a temperature controller (ITC503S; Oxford Instruments). Data were fit using gaussian distributions, as implemented in the DEERAnalysis2008 package (21).

Structural Refinement—The crystal structure of the rat endophilin dimer (Protein Data Bank code 2C08) (5) was used as a starting point for computational refinement based on distance and depth constraints derived from EPR data. A complete description of the details of this procedure is given in the supplemental material. An in-house algorithm (PRONOX) was used to add residues 64–86 to each subunit of the endophilin dimer: add spin labels at positions 63, 66, 70, 73, 74, 75, 77, and 83; locate the starting structure at the surface of an imaginary lipid vesicle; and produce a set of constraints for simulated annealing molecular dynamics (SAMD) calculations. Based on the secondary structure determined by EPR, residues 64–75 were built as helices and constrained using hydrogen-bonding constraints to maintain a helical structure. These constraints, interdimer distance constraints measured from continuous wave EPR and four-pulse DEER EPR, lipid depths for residues 63, 66, and 70, and other system constraints (supplemental Tables S1 and S2) were used in SAMD simulations in AMBER8 (22). During these calculations, the helix and loop were not covalently linked to each other or to the BAR domain to allow

Membrane Curvature Generation

TABLE 1

Intra- and intersubunit distances between spin-labeled residues in membrane-bound endophilin measured by EPR

Distances obtained from continuous wave (CW) or four-pulsed DEER experiments (DEER) were fit using gaussian models (Fig. 1 and [supplemental Fig. S1](#)). All distances were obtained for the indicated endophilin derivatives bound to membrane. The experimental distances are given as the peak of the gaussian distributions and are in good agreement with distances expected from the crystal structure which was taken as the α -carbon distance between the indicated residues.

Mutant	EPR distance	Crystal structure
	\AA	\AA
227R1	9 (CW)	8
63R1	9 (CW)	11
96R1	38 (DEER)	36
216R1	37 (DEER)	34
166R1-210R1	43 (DEER)	35
178R1-200R1	31 (DEER)	33

freedom of movement according to the distance and depth constraints. Sixty cycles of SAMD were performed starting from a conformation with the helical axes approximately orthogonal to the long axis of the BAR domain. The motion of the insert helices (residues 64–75 in each subunit) was monitored by calculation of the angle between the helical axis and the long axis of the BAR domain (see [the supplemental material](#)). The lipid vesicle was built as described previously (23).

RESULTS

Rat Endophilin A1-BAR Is a Dimer upon Membrane Interaction—To investigate whether the BAR domain of the rat endophilin A1 dimer observed crystallographically is retained upon membrane interaction, we generated a series of spin-labeled endophilin derivatives (Fig. 1A) and incubated them with liposomes comprised of Folch lipids. The experimental conditions were chosen such that the Folch liposomes were predominantly vesiculated into highly curved vesicles with an average diameter of ~ 230 \AA , as determined by electron microscopy ([supplemental Fig. S1A](#)). We then measured intra- and intersubunit distances and compared them with the respective α -carbon distances of the crystal dimer. The distances measured by EPR are those between the nitroxide moieties of R1, and therefore, they would be expected to be similar but not necessarily identical to the α -carbon distances. Distances >20 \AA were investigated using four-pulse DEER (24–27), whereas shorter distances were investigated using continuous wave EPR (28, 29) (see “Experimental Procedures”).

The DEER measurements are illustrated with the example of membrane-bound endophilin spin-labeled in helix 3 at position 216 (Fig. 1A). A pronounced periodic oscillation is observed for this 216R1 derivative (Fig. 1B), and frequency analysis of this oscillation yields a well defined distance distribution with a maximum at 37 \AA (Fig. 1C). This distance is in good agreement with the respective intersubunit α -carbon distance of 34 \AA in the crystal structure of endophilin (Table 1). Similarly, the intradimer distances of membrane-bound 96R1 (in helix 1b), 63R1 (in the helix 1 insert), and the previously reported (5) distance for 227R1 (in helix 3) are in good agreement with the crystal structure (Table 1 and [supplemental Fig. S1, B and C](#)). As a control, we also measured the intersubunit distance for one of the derivatives (96R1) in solution and obtained the same dis-

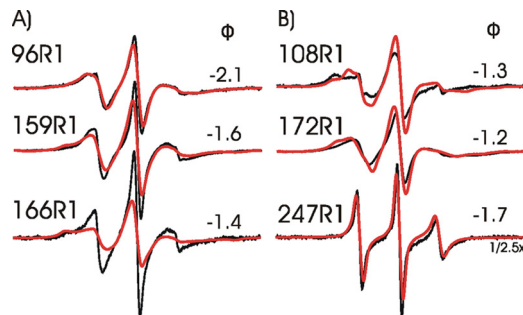


FIGURE 2. EPR analysis of sites in the BAR domain. Continuous wave X-band EPR spectra of soluble (black) and membrane-bound (red) endophilin derivatives spin-labeled positions on (A) or facing away from the concave surface (B). All spectra were normalized to the same number of spins. Spectra for 247R1 were of much higher intensity and, therefore, were shown at 2.5-fold reduced intensity. The scan width is 100 gauss. The depth parameter (Φ) values for all derivatives in membrane-bound form are strongly negative (less than -1), indicating that the respective spin-labeled sites do not significantly penetrate into the hydrocarbon layer of the membrane.

tance as that for the membrane-bound form ([supplemental Fig. S1D](#)).

The tip-to-tip distance of the endophilin dimer in the crystal is nearly 130 \AA . Because this range is beyond the detection limit for intersubunit contacts, we employed a different approach and measured distances between two sites located toward the tip region in the same subunit. As shown in Table 1 and [supplemental Fig. S1B](#), the distance of 31 \AA between 178R1 and 200R1 (located directly at the tip and in helix 3, respectively) is also in good agreement with the α -carbon distances of the crystal structure (33 \AA). It has been found previously that the structures of different families of BAR domain proteins overlay well in the central region but are much more divergent toward the tips or wings (15). To test for potential movement between the central region and the wing region, we measured the distance between 166R1 and 210R1 (located in helix 2 and 3, respectively). The distance between these residues for membrane-bound endophilin is in good agreement with the expected distance from the crystal structure (Table 1 and [supplemental Fig. S1B](#)). Moreover, the same distance was obtained when distances were measured between these residues in solution ([supplemental Fig. S1D](#)). Collectively, this distance analysis supports the notion that the overall structure of the BAR domain dimer is largely retained upon membrane interaction.

Concave Surface of the BAR Domain Does Not Penetrate Deeply into the Acyl Chain Interior of the Membrane—Next, we used mobility and accessibility analysis of selected spin-labeled derivatives to investigate the mechanisms by which the BAR domain interacts with the membrane. Spin labels were introduced at positions that were either located on the concave surface of the BAR domain (positions 96, 159, and 166) or at positions expected to face away from the membrane (positions 108, 172, and 247) (Fig. 1A).

The EPR spectra for these derivatives in the soluble (black trace, Fig. 2) and membrane-bound forms (red trace, Fig. 2) are qualitatively similar and consistent with the respective locations in the crystal structure. For example, the EPR spectra for 247R1 (Fig. 2B) are characterized by three sharp and narrowly spaced lines in both conditions. The high motion indicated by these spectra is consistent with the location of this site at the C



FIGURE 3. EPR spectra for residues located in the helix 1 insert indicate ordering of the region in the presence of membrane. Spectra for soluble (black) and membrane-bound (red) endophilin derivatives are shown. The line broadening and loss of spectral amplitude of all sites upon membrane interaction reflect, to a significant extent, a reduction in mobility and ordering. Additional broadening from spin–spin interaction between the same sites only has minor spectral contributions because the labeled sites are relatively far apart (also see discussion of Table 2). Scan width is 100 gauss.

terminus of a helix that is likely to be frayed in solution. However, some membrane binding-induced immobilization is detected for 159R1 and 166R1. The immobilization observed at those sites could be caused by a direct interaction with the lipids or other regions of the proteins. We note that both sites could be in proximity to the membrane-embedded N-terminal helix 0 or the linker that connects it to helix 1 (5).

To investigate the proximity of the labeled sites to the membrane bilayer, we used accessibility of the labels to the paramagnetic colliders, O_2 and NiEDDA. Although the concentration of the nonpolar O_2 increases in the membrane, the more polar NiEDDA preferentially partitions into the solvent. Thus, the deeper a spin label penetrates into the acyl chain region, the more it becomes accessible to O_2 and inaccessible to NiEDDA. The accessibilities to O_2 and NiEDDA (ΠO_2 and $\Pi NiEDDA$) are conveniently summarized by the depth parameter Φ ($\Phi = \ln(\Pi O_2 / \Pi NiEDDA)$). Interestingly, the Φ values for positions 96, 159, and 166 (on the concave face) or 108, 172, and 247 (toward the convex face) were all in the range from -1.2 to -2.1 (Fig. 2). Thus, the depth parameter Φ indicates little membrane penetration by residues on the concave surface of the BAR because the values of Φ do not differ between labels at three such positions and those at solvent-exposed positions. Although these data clearly indicate the lack of significant acyl chain penetration of the nitroxide moiety of the spin-labeled sites, they do not exclude the possibility that the concave surface of endophilin interacts with the interfacial region of the bilayer (see below).

Central Insert Region Becomes an Amphipathic Helix upon Membrane Interaction—To investigate potential membrane-induced conformational changes in the helix insert region, we conducted a nitroxide scanning experiment. The EPR spectra of the soluble derivatives (Fig. 3, black) are generally of higher

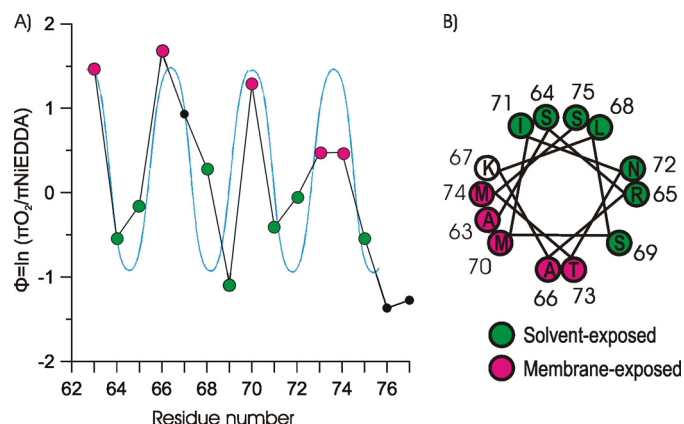


FIGURE 4. Depth parameter Φ plotted as function of residue number. The accessibility of membrane-bound endophilin derivatives to NiEDDA and O_2 ($\Pi NiEDDA$ and ΠO_2) was determined using power saturation, and Φ was calculated according to $\Phi = \ln(\Pi O_2 / \Pi NiEDDA)$. *A*, when plotted as function of labeling position, Φ exhibits a periodic oscillation (for residues 63–75) corresponding to that of an α -helix as illustrated with the sinusoidal line which has a periodicity of 3.6 amino acids/turn. *B*, membrane-exposed sites (red maxima) fall onto one face of a helical wheel, whereas the solvent-exposed sites (green minima) fall onto the opposite face of a helical wheel.

amplitude with sharper spectral lines than those from the respective membrane-bound forms (Fig. 3, red). Control experiments, in which sucrose was used to slow down the tumbling of the dimer in solution, showed little spectral changes, indicating that the membrane binding-induced change in tumbling rate did not play a significant spectral role (data not shown). The line shapes of 70R1 to 77R1 indicate a largely disordered and unfolded structure in solution, whereas a more ordered structure is induced upon membrane binding. Only residues 64–69 are ordered in solution, and pronounced immobilization can be seen for 64R1, 65R1, 68R1, and 69R1. Such immobilization could be caused by tertiary contacts. This region was largely disordered in the crystal structure of rat endophilin (5) but was resolved in the structure of human endophilin (8), in which residues 63–70 were found to form a short helical segment. Moreover, residues 64, 65, 68, and 69 are pointing directly toward the BAR domain in the latter structure. Thus, the EPR spectra in the absence of membranes are consistent with a structure akin to that in the crystal of human endophilin (also see below). Residues 64–69 are also the most ordered region of the membrane-bound form, but in the presence of membranes the ordered region becomes much more extended.

To obtain more detailed secondary structure information in the membrane-bound form, we performed O_2 and NiEDDA accessibility measurements for 63R1 to 77R1. As summarized with the depth parameter Φ (Fig. 4*A*), the accessibility data give rise to a periodic oscillation. The local Φ -maxima (residues 63, 66, 70, 73, and 74; magenta) represent preferentially O_2 accessible, lipid-exposed sites, and these positions cluster on the hydrophobic face of a helical wheel (Fig. 4*B*). Conversely, the local minima (green) correspond to solvent-exposed sites that fall onto the opposite face of the helical wheel. The formation of an amphipathic α -helical structure is further supported by a comparison of the Φ -data with a cosine curve that has the standard periodicity of an α -helix (3.6 amino acids/turn). This curve agrees well with the experimentally observed periodicity from residues 63 to 75, but it starts to diverge for residues 76

Membrane Curvature Generation

TABLE 2

Intramolecular distances between same sites in the insert region of membrane-bound endophilin

Distances were obtained by four-pulse DEER (supplemental Fig. S2) or continuous wave (CW) EPR (supplemental Fig. S1C). The experimental distances shown in the table correspond to the intermolecular distances between same sites within the dimer. The distances increase with increasing residue number, indicating an antiparallel arrangement of the helices.

Mutant	Experimental distance
	Å
63R1	9 (CW)
64R1	18 (DEER)
65R1	24 (DEER)
66R1	19 (DEER)
67R1	23 (DEER)
70R1	28 (DEER)
71R1	37 (DEER)
73R1	41 (DEER)
74R1	44 (DEER)
75R1	42 (DEER)
77R1	49 (DEER)
83R1	44 (DEER)

and 77. For these residues, an increase in the Φ -values would be predicted, but the opposite is observed. Thus, these residues may no longer be part of the helix.

Previous studies demonstrated that Φ -values are proportional to the membrane immersion depth of R1 side chains that are penetrating into the acyl chain region. This depth can be calibrated using spin-labeled derivatives of phospholipids (20, 30). Based on such a calibration (see “Experimental Procedures”), we obtain average immersion depths of the nitroxide moieties of 63R1, 66R1, and 70R1 that are on the order of 5–6 Å. Previous work has shown that an R1 side chain is typically at a distance of 7–10 Å from the center of an α -helix to which it is attached (31). Thus, we can estimate that the center of the helix is located about 1–4 Å above the phosphate layer. The Φ -values for residues 73 and 74 are somewhat lower, and the reduced immersion depth of these sites is consistent with a slight helix tilt. However, residues 73 and 74 are also located on the periphery of the hydrophobic face (Fig. 4B) where the side chains might project laterally rather than directly toward the bilayer interior.

Dimeric Amphipathic Helices in the Central Insert Region Are Antiparallel—To analyze the orientation of the amphipathic helices with respect to each other, we measured intersubunit distances between the same sites in each subunit using DEER (supplemental Fig. S2). As shown in Table 2, the distance between these sites generally increases with increasing residue number, indicating that the helices must be facing away from each other. This feature is best illustrated with the lipid-exposed sites 63R1, 66R1, and 70R1. For these sites, we can assume that the nitroxide side chains are facing in the same direction (*i.e.* into the membrane) and that the interlabel distances are likely to be close to those between the respective α -carbon atoms. An interesting feature of the DEER distances is that they increase by about 10 Å for each helical turn, which is in good agreement with antiparallel helices because an individual helix is extended by ~5 Å/turn. The other distances in Table 2 are also in agreement with a helical structure (also see below).

Since Masuda and colleagues (8) observed a short antiparallel helical structure for residues 63–71 in the crystal structure of human endophilin A1, we sought to determine whether the distances in solution are similar to those in the membrane-

bound form. As shown in supplemental Table S3, the intersubunit distances for 63R1, 67R1, and 70R1 in the absence of membranes differ from those observed in the membrane-bound state. Compared with the α -carbon distances from the crystal structure, the measured distances in solution are in good agreement. These data suggest that the structure of the insert taken up in the crystal of human endophilin A1 is similar to that of rat endophilin A1 in solution and that the structure taken up in the membrane-bound state is different.

Structural Refinement of the Central Insert Suggests Staggered Helices with High Mobility—To generate atomistic models of the membrane-bound form of endophilin, we used the crystal structure of the soluble rat endophilin A1 dimer as a starting structure and built and refined the structure of the insert region (residues 63–86) using a modified version of our previously reported (23) SAMD refinement constrained by the EPR results. These calculations included intersubunit constraints based on DEER distances, depth constraints based on EPR accessibility data, constraints to maintain the helicity of the insert region as detected by EPR mobility and accessibility data, and symmetry constraints on the insert regions of the two subunits. The intersubunit constraints were implemented as the mean distance ± 5 Å to reflect the relatively large width of the EPR distance distributions.

Endophilin structures were collected at the end of each of 60 SAMD cycles. The insert helices clearly adopted one of three positions with an angle between the helical axis and the long axis of the BAR domain of about 140°, 90°, and 40°, respectively (supplemental Fig. S3), with 18, 33, and 9 occurrences, respectively, over the 60 SAMD cycles. The three positions of the insert helices are interconvertible, and all may occur in a population of membrane-bound endophilin proteins. This may account for the width of the distance distribution for the intersubunit DEER data. However, in the SAMD cycles shown in supplemental Fig. S3A and in other calculations performed with minor changes in parameters (see the supplemental material), we consistently find that the most common conformation is that with the insert helices orthogonal to the BAR domain axis (green helices in supplemental Fig. S3B).

To examine the interaction of the endophilin dimer with a curved lipid surface, we used a representative structure with orthogonal insert helices and constructed part of a lipid vesicle around the protein (Fig. 5). We were able to do this because the predicted structure is positioned in space based on depth constraints relating the center of the lipid vesicle to the protein. Two main findings for the insert helices emerge from the SAMD calculations and subsequent building of the lipid surface. First, the helices (residues 63–75) are tilted such that the N terminus of each helix is located below the phosphate of the lipid head group, whereas the C terminus and the loop (residues 76–86) are positioned above the lipid surface (Fig. 5B). Second, the axes of the helices adopted a staggered position with respect to each other (Fig. 5A).

The detailed positions of amino acids 63–75 are shown in Fig. 5C. The amino acid positions obtained by computational refinement using EPR distance, depth and mobility data, and geometrical and symmetry constraints show remarkably good agreement with the predicted orientations based on ac-

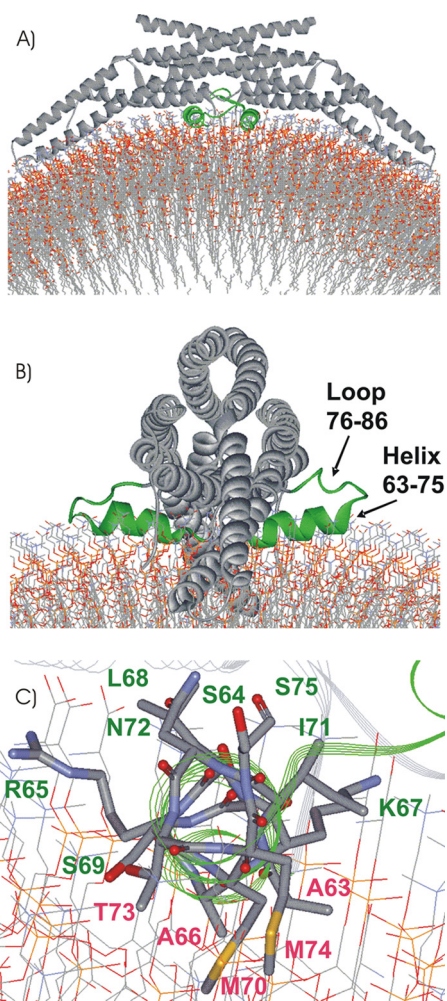


FIGURE 5. Images of an endophilin dimer docked to a lipid vesicle of 11 Å radius (measured to the P atom of the head group). Shown are the BAR domain, the insert region, and parts of the phospholipid vesicle. The N-terminal helices are not shown because its precise location relative to the BAR domain has not yet been determined. *A*, side view of the protein illustrating insertion of the insert helices (green) into the lipid and the fit of the BAR domain scaffold to the lipid vesicle. *B*, view looking down the long axis of the BAR domain, showing the tilt of the insert helices (green, residues 63–75). The N terminus of each helix is located below the level of the P atoms (orange) of the lipid head groups, whereas the C terminus is positioned above the lipid surface. The loop of the insert (green line, residues 76–86) is also located above the lipid surface. *C*, insert helix in one subunit, viewed from the C terminus of the helix (orientation similar to that in *A*). Amino acids are identified in red (below the phosphate) and green (above the phosphate), consistent with the nomenclature in Fig. 4.

cessibility data only (Fig. 4). Hence, Ala-63, Ala-66, Met-70, Thr-73, and Met-74 are oriented into or toward the hydrophobic region of the lipids. All of the remaining side chains are positioned above the phosphate head groups and may be considered in three categories. First, Arg-65 and Lys-67 are oriented sideways from the helix and can interact with negative charges on the lipid head groups. Second, three serine residues and Asn-72 are either solvent-exposed or hydrogen-bonded to head groups, and these residues produce an element of amphipathicity in the helix. Third, Leu-68 and Ile-71 are two hydrophobic residues that apparently break this amphipathicity. However, the side chain of Leu-68 forms hydrophobic contacts with Ile-55 and Leu-58 in the BAR domain. This interaction, as well as the interaction between Ile-71 and Tyr-86 may

help to stabilize the orthogonal orientation of the insert helices (supplemental Fig. S4).

DISCUSSION

In this study, we investigated the structure of endophilin bound to small and highly curved vesicles. Under these conditions, the BAR domain of endophilin retains a dimeric structure similar to that found in the crystal. This demonstrates that endophilin does not undergo major conformational refolding upon membrane binding, unlike the case of annexin B12 (19). Moreover, we find that a central insert region (residues 63–75) becomes helical and inserts into the membrane at an immersion depth that is comparable (albeit slightly shallower) to that of the N-terminal helix (5). The insert helix in each subunit is tilted such that the side chains of Ala-63 and Ala-66 at the N terminus are below the level of the phosphate head groups of the lipid. The position of this helix with respect to the BAR domain is flexible, but seems to adopt a preferential position with the helical axes orthogonal to the BAR domain long axis.

The width of the DEER distance distributions for intersubunit distances between residues in the insert helices suggested some structural heterogeneity. This manifested in the computational refinement as three distinct positions with angles of about 140°, 90°, and 40° between the helical axis and the BAR domain. Interestingly, the 40° position is very close to the position adopted by the insert helices in the x-ray structure of human endophilin (8). In this crystal structure, Arg-65 in the insert helix forms a salt bridge with Glu-56, and a similar salt bridge forms in the 40° structures obtained in our SAMD refinement (supplemental Fig. S5A). In an analogous manner, Lys-67 in the insert helix forms a salt bridge with Glu-56 (in the opposite subunit) in the 140° structures generated in the SAMD calculation (supplemental Fig. S5B), whereas the salt bridge between Arg-65 and Glu-56 (same subunit) is broken. In the orthogonal structures, neither Arg-65 nor Lys-67 is located close enough to Glu-56 in the same or the opposite subunit, and the positive charges are therefore free to interact with the lipid head groups (supplemental Fig. S5C). Thus, a picture emerges of a dynamic helix that might occupy a range of conformations based on these electrostatically favorable interactions. It appears that the orthogonal orientation should be favorable in the membrane-bound state, but the other orientations of the helix might be accessible to adjust to different membrane and curvature conditions. This behavior and the detailed orientations of the side chains of the helices may be amenable to analysis by theoretical calculations along the lines of those performed previously for membrane-bound endophilin (17).

Two mechanisms have been suggested by which insertion of amphipathic helices can induce curvature. By inserting helices into only the outer leaflet of the bilayer, an imbalance is created between the two leaflets, and the tighter packing in the outer leaflet causes an expansion that, in turn, leads to bending of the membrane. In addition, insertion of helices at the level of the head groups could induce additional curvature strains by preferentially increasing the packing density in the head group rather than the acyl chain region (32). In the case of membrane-inserted amphipathic helices, these mechanisms are expected to promote membrane curvature in a direction perpendicular

Membrane Curvature Generation

to that of the helix axis. Thus, the antiparallel insert helices in their most predominant orientation are ideally positioned to induce curvature along the concave surface of the BAR domain.

In contrast, the Φ -values for sites labeled on the concave surface of the BAR domain did not indicate penetration into the acyl chain region, and the endophilin BAR domain must, therefore, be positioned farther away from the membrane than its amphipathic helices. Thus, if the concave surface of endophilin interacts with the bilayer, it likely does so by interaction with the more distal portions of the head group. This general behavior is consistent with the model in Fig. 5, in which the BAR domain is docked onto a lipid vesicle according to the immersion depth information obtained for the insert helix. In this model, the BAR domain follows the general shape of the vesicle and is positioned to interact with the outer region of the membrane head groups. Future studies will have to show whether the structural features found under the present lipid conditions will also apply to vesicles of different sizes or to tubules.

REFERENCES

1. McMahon, H. T., and Gallop, J. L. (2005) *Nature* **438**, 590–596
2. Zimmerberg, J., and Kozlov, M. M. (2006) *Nat. Rev. Mol. Cell Biol.* **7**, 9–19
3. Farsad, K., Ringstad, N., Takei, K., Floyd, S. R., Rose, K., and De Camilli, P. (2001) *J. Cell Biol.* **155**, 193–200
4. Ford, M. G., Mills, I. G., Peter, B. J., Vallis, Y., Praefcke, G. J., Evans, P. R., and McMahon, H. T. (2002) *Nature* **419**, 361–366
5. Gallop, J. L., Jao, C. C., Kent, H. M., Butler, P. J., Evans, P. R., Langen, R., and McMahon, H. T. (2006) *EMBO J.* **25**, 2898–2910
6. Peter, B. J., Kent, H. M., Mills, I. G., Vallis, Y., Butler, P. J., Evans, P. R., and McMahon, H. T. (2004) *Science* **303**, 495–499
7. Frost, A., Perera, R., Roux, A., Spasov, K., Destaing, O., Egelman, E. H., De Camilli, P., and Unger, V. M. (2008) *Cell* **132**, 807–817
8. Masuda, M., Takeda, S., Sone, M., Ohki, T., Mori, H., Kamioka, Y., and Mochizuki, N. (2006) *EMBO J.* **25**, 2889–2897
9. Weissenhorn, W. (2005) *J. Mol. Biol.* **351**, 653–661
10. Arkhipov, A., Yin, Y., and Schulten, K. (2008) *Biophys. J.* **95**, 2806–2821
11. Ayton, G. S., Blood, P. D., and Voth, G. A. (2007) *Biophys. J.* **92**, 3595–3602
12. Ayton, G. S., Lyman, E., Krishna, V., Swenson, R. D., Mim, C., Unger, V. M., and Voth, G. A. (2009) *Biophys. J.* **97**, 1616–1625
13. Blood, P. D., and Voth, G. A. (2006) *Proc. Natl. Acad. Sci. U.S.A.* **103**, 15068–15072
14. Frost, A., De Camilli, P., and Unger, V. M. (2007) *Structure* **15**, 751–753
15. Henne, W. M., Kent, H. M., Ford, M. G., Hegde, B. G., Daumke, O., Butler, P. J., Mittal, R., Langen, R., Evans, P. R., and McMahon, H. T. (2007) *Structure* **15**, 839–852
16. Yin, Y., Arkhipov, A., and Schulten, K. (2009) *Structure* **17**, 882–892
17. Cui, H., Ayton, G. S., and Voth, G. A. (2009) *Biophys. J.* **97**, 2746–2753
18. Jung, A. G., Labarerra, C., Jansen, A. M., Qvortrup, K., Wild, K., and Kjaerulff, O. *PLoS One* **5**, e9492
19. Fischer, T., Lu, L., Haigler, H. T., and Langen, R. (2007) *J. Biol. Chem.* **282**, 9996–10004
20. Altenbach, C., Greenhalgh, D. A., Khorana, H. G., and Hubbell, W. L. (1994) *Proc. Natl. Acad. Sci. U.S.A.* **91**, 1667–1671
21. Jeschke, G., Chechik, V., Ionita, P., Godt, A., Zimmermann, H., Banham, J., Timmel, C. R., Hilger, D., and Jung, H. (2006) *Appl. Magn. Reson.* **30**, 473–498
22. Case, D. A., Darden, T. A., Cheatham, T. E. III, Simmerling, C. L., Wang, J., Duke, R. E., Luo, R., Merz, K. M., Wang, B., Pearlman, D. A., Crowley, M., Brozell, S., Tsui, V., Gohlke, H., Mongan, J., Hornak, V., Cui, G., Beroza, P., Shafmeister, C., Caldwell, J. W., Ross, W. S., and Kollman, P. A. (2004) *AMBER 8*, University of California, San Francisco
23. Jao, C. C., Hegde, B. G., Chen, J., Haworth, I. S., and Langen, R. (2008) *Proc. Natl. Acad. Sci. U.S.A.* **105**, 19666–19671
24. Altenbach, C., Kusnetzow, A. K., Ernst, O. P., Hofmann, K. P., and Hubbell, W. L. (2008) *Proc. Natl. Acad. Sci. U.S.A.* **105**, 7439–7444
25. Bhatnagar, J., Freed, J. H., and Crane, B. R. (2007) *Methods Enzymol.* **423**, 117–133
26. Jeschke, G., and Polyhach, Y. (2007) *Phys. Chem. Chem. Phys.* **9**, 1895–1910
27. Pannier, M., Veit, S., Godt, A., Jeschke, G., and Spiess, H. W. (2000) *J. Magn. Reson.* **142**, 331–340
28. Altenbach, C., Oh, K. J., Trabertino, R. J., Hideg, K., and Hubbell, W. L. (2001) *Biochemistry* **40**, 15471–15482
29. Rabenstein, M. D., and Shin, Y. K. (1995) *Proc. Natl. Acad. Sci. U.S.A.* **92**, 8239–8243
30. Frazier, A. A., Wisner, M. A., Malmberg, N. J., Victor, K. G., Fanucci, G. E., Nalefski, E. A., Falke, J. J., and Cafiso, D. S. (2002) *Biochemistry* **41**, 6282–6292
31. Langen, R., Oh, K. J., Cascio, D., and Hubbell, W. L. (2000) *Biochemistry* **39**, 8396–8405
32. Campelo, F., McMahon, H. T., and Kozlov, M. M. (2008) *Biophys. J.* **95**, 2325–2339

Simulated Annealing Molecular Dynamics

Structure Building

The X-ray coordinates of the rat endophilin A1 dimer (PDB ID 2C08) were used as a starting point for model building. Each monomer in this structure includes residues 25-247 with a 19-amino acid gap from residues 68 to 86. Protons were added using the LEAP module in AMBER8. Each monomer was then modified by addition of 23 amino acids (SRAKLSMINTMSKIRGQEKGPGY, residues 64-86; residues 64-67 in the original structure were deleted). Residues S64 to M74 (the putative α -helix insert) were built with torsional angles of phi = -57° and psi = -47°, and residues S75 to Y85 (a putative loop region) had phi = 180° and psi = 180°. The psi angle for A63 was included as 0°, which gives a starting orientation with the S64-M74 α -helix axis approximately orthogonal to the long axis of the BAR domain (see below).

An in-house algorithm (PRONOX) was used to generate the labeled structure, to position the starting structure at the surface of an imaginary lipid vesicle, and to produce a set of constraints for the simulated annealing molecular dynamics (SAMD) calculations. PRONOX is a stand-alone algorithm for flexible construction of input files for simulated annealing. Eight spin labels were added to each monomer at residues 63, 66, 70, 73, 74, 75, 77 and 83. The first six of these labels were added in the *m,m* conformation (1) to residues in the helical region, and the last two were added in the *m,t* conformation to residues in the (initially extended) loop region.

The initial position of the BAR domain with added helices and loops was determined with respect to a lipid vesicle of 115 Å radius (the distance from the sphere center to the phosphorus atom of the head group of the lipid in the outer leaflet). The BAR domain was positioned such that the midpoint between Y57(C α) in each monomer was 10 Å above the sphere circumference (the level of the P atom of each headgroup). Y57(C α) was chosen since the line connecting the two atoms in the dimer is approximately parallel to the long axis of the BAR domain. The position of the BAR domain was based on EPR data for residues 96, 159, and 166, as discussed in the main text.

Simulated Annealing Molecular Dynamics (SAMD)

SAMD calculations were performed in AMBER8. Preliminary calculations indicated that the most effective approach was to include breaks between residues P62 and A63R1 (the point of connection of the BAR domain and the helix), S75R1 and K76 (the putative joint of the helix and the loop; residue 75 was retained in the helical region based on the EPR data in Fig. 4), and Y86 and P87 (the connection of the loop back to the BAR domain). These breaks are included simply by addition of “TER” lines at the appropriate positions in the input PDB file, and with no changes in geometry or deletion or addition of atoms. From the perspective of the force field, each TER indicates termination of a protein chain, and so the calculation proceeds as a simulation of a series of disconnected protein segments (but with constraints to prevent the segments moving too far from each other; see below).

After a brief minimization of the starting structure, two equilibration cycles were performed with loose constraints on the “missing” peptide bonds (< 13 Å and < 8 Å in preliminary cycles 1 and 2, respectively). These cycles were performed for 60 ps each at a constant temperature of 298K (i.e., no simulated annealing), a time step of 0.002 ps, and the other constraints shown in Table S2. In the preliminary cycles, the position of

P60, N61 and P62 were fixed. All other conditions were similar to those described for the SAMD cycles in the following paragraphs.

The two preliminary cycles were followed by 60 cycles of SAMD performed for 60 ps / cycle. The “missing” peptide bonds were constrained to distances < 5 Å and these and other constraints were implemented as shown in Table S2. This approach allows flexible motion of the putative helix and loop regions, but inclusion of distance constraints for the “missing” peptide bonds provides a limitation on the flexibility. We also imposed symmetry onto the insert region by inclusion of torsional constraints defined between equivalent C α atoms in each subunit, using two “dummy atoms” positioned above and below the protein on an axis orthogonal to the long axis of the BAR domain. The P60-P62 (linker from the bar domain to the helix), A63R1-S75R1 (helix) and K76-Y86 (loop) of each subunit were free to move in the SAMD calculations. The position and structure of the BAR domain were fixed.

Each SAMD cycle included a heating phase from 0K to 1200K in 8 ps, during which the force constants for the constraints were increased from 0.1 to 10.0; maintenance of the temperature at 1200K for a further 12 ps; and then cooling to 0K over 40 ps, with stepwise adjustments of the TAUTP parameter. This approach was based on the standard recommended protocol for simulated annealing calculations in the AMBER8 manual (2) and on our approach to refinement of the lipid-bound alpha-synuclein structure (3). The molecular dynamics was performed with a time step of 0.002 ps, a distance dependent dielectric of 4, and a cut-off of 10.0 Å.

The “atom” representing the center of the imaginary lipid vesicle was constrained to the origin with a force constant of 1000.0 kcal/mol/Å. In the SAMD simulation, the lipid vesicle is a sphere with which the starting position of the protein has a defined geometrical relationship, thereby allowing inclusion of the EPR depth data as constraints in the calculation. This relationship is established in PRONOX through rotation and translation of the protein with respect to the sphere. In the SAMD calculation, there are no explicit lipid molecules included. However, PRONOX can build a molecular representation of the lipid bilayer that is consistent with the curvature of the sphere and sterically consistent with the position and conformation of the protein determined in the SAMD calculations. Therefore, images of the location of the protein in the lipid can be generated after the SAMD procedure is completed.

Structures were collected at the end of each SAMD cycle, giving a total of 60 structures. Each of these was processed further to connect the missing peptide bonds. AMBER8 forcefield parameters for the bonds were included and then residues 60 to 86 of each subunit were subjected to a brief minimization of 1000 steps, a 1 ps simulation at low temperature (raised from 0 to 100 K over 1 ps), and then a final minimization for 1000 steps. The simulation was performed using the same constraints as those in the SAMD calculation, with additional torsional angle constraints on the new peptide linkages to ensure that a trans conformation was achieved around these bonds. All structures were checked for correct chirality and trans configurations around the peptide bonds. In the image shown in Fig. 5, the conformations of the side chains of M70, T73 and M74 were adjusted (while maintaining staggered conformers around side chain bonds) to give orientations consistent with the EPR data and the chemistry of the side chain.

Full details of the PRONOX and AMBER input files and the force field parameters used to perform the SAMD calculations will be provided on request. The executable for the PRONOX algorithm will also be made available on request.

Structure Analysis

The motion of the S64-M74 helices in the SAMD calculation was monitored using an angle between the helical axis and a line parallel to the long symmetry axis of the BAR domain (Fig. S3). This angle was defined as C α (residue 74)-C α (67)-C α (182), where C α (74)-C α (67) is an approximation of the helical axis and C α (182) was chosen such that the calculated angle was close to 90° when the S64 to M74 helix was approximately orthogonal to the BAR domain axis. For visualization, the structures were overlaid in WebLab Viewer.

Additional Calculations

Further sets of SAMD calculations were performed with variation of the position of the BAR domain, the starting position of A63 psi (-47°), variation of the force constants applied to the symmetry constraints, and/or elimination of the symmetry constraints, but otherwise identical conditions to those for the calculations described above. Similar behavior of the S64-M74 helices was observed in these calculations, with adoption of the three general helical orientations described above. The only exception was the calculation run without symmetry constraints in which, as expected, the helices moved independently of each other and asymmetrical structures were generated. However, each helix still adopted one of the three orientations identified in the symmetry-constrained calculations.

References

1. Guo, Z., Cascio, D., Hideg, K., and Hubbell, W. L. (2008) *Protein Sci* **17**(2), 228-239
2. Case, D. A., Darden, T. A., Cheatham, I., T.E., Simmerling, C. L., J., W., Duke, R. E., Luo, R., Merz, K. M., Wang, B., Pearlman, D. A., Crowley, M., Brozell, S., Tsui, V., Gohlke, H., Mongan, J., Hornak, V., Cui, G., Beroza, P., Shafmeister, C., Caldwell, J. W., Ross, W. S., and Kollman, P. A. (2004) *AMBER 8*, University of California, San Francisco
3. Jao, C. C., Hegde, B. G., Chen, J., Haworth, I. S., and Langen, R. (2008) *Proc Natl Acad Sci U S A* **105**(50), 19666-19671
4. Gross, A., Columbus, L., Hideg, K., Altenbach, C., and Hubbell, W. L. (1999) *Biochemistry* **38**(32), 10324-10335

Table S1. Label depths used in SAMD calculations.

Label	Measured Depth (Å) ¹	Distance from Center (Å) ²
63	5.4	109.6
66	6.6	107.4
70	4.2	110.8

¹ Depth of the label below the phosphate group of the lipid based on EPR accessibility

data and depth calibration using spin-labeled lipids (see methods).

² Distance from the label (assumed to be from the N atom of the nitroxide group) to the center of an imaginary lipid vesicle of diameter 230 Å. This value is calculated as 115 Å – N Å, where N is the measured depth and 115 Å is the radius.

Table S2. Constraints used in SAMD calculations.

Geometry Element	Structural Element in Each Monomer	Value ¹	r1 ²	r2 ²	r3 ²	r4 ²
Inter-label distance	Labels at 63, 66, 70, 73, 74, 75, 77, 83	Exptl. N (Å)	N-6	N-5	N+5	N+6
Label-vesicle center distance	Labels at 63, 66, 70	Exptl. N (Å)	N-3	N-2.5	N+2.5	N+3
Backbone H-bond distance	Residues 63 to 75 (helix)	2.15 Å	1.3 Å	1.8 Å	2.5 Å	3.0 Å
H α – S δ distance	Labels	2.8 Å	1.8 Å	2.3 Å	3.3 Å	3.8 Å
Peptide bond breaks	Bonds connecting 62-63, 75-76, 86-87	< 5.0 Å	1.4 Å	1.5 Å	3.0 Å	5.0 Å
Symmetry ³	Residues 63 to 86 C α - D α - D α - C α ³	180°	177°	178°	182°	183°

¹ The value is either experimental (see Table 1 for DEER inter-label distances and Table S1 for depth data) or an idealized value for the particular geometry element.

² The values for r1 to r4 define the limits of the potential function used for inclusion of constraints in simulated annealing in AMBER (2).

³ D α = dummy atom. Details are given in the supplementary text.

Table S3. Intra-dimer distances in membrane-bound and soluble endophilin derivatives obtained from continuous wave (CW) or pulsed (DEER) EPR. The distances are compared to the α -carbon distances obtained crystallographically.

Mutant	EPR distance (\AA) membrane	EPR distance (\AA) solution	Crystal structure (\AA)
63R1	9 (CW)	9 (CW)	12
66R1	19 (DEER)	24 (DEER)	23
70R1	28 (DEER)	35 (DEER)	35

Supplemental Figure Legends

Figure S1. Membrane Interaction of endophilin A1 monitored by electron microscopy and EPR. (A) Negative stain image of endophilin A1 incubated with Folch liposomes for 20 minutes at room temperature. The original size of the vesicles was ~400nm, but after the addition of endophilin A1, vesicle diameters are 23 nm on average. Scale bar is 100nm. Folch liposomes before incubation with endophilin contained mostly large liposomes. (B) 4-pulse DEER data obtained for membrane-bound endophilin derivatives. The baseline subtracted data are shown in black, while the Gaussian fits are shown in red. The distance distribution corresponding to the observed oscillation is given in the right column. In order to further verify that the measured distances for doubly labeled derivatives were within a given subunit, DEER data were also obtained from samples in which spin labeled protein was diluted with excess of wild-type protein and comparable results were obtained (data not shown). (C) Comparison of the continuous wave EPR spectra for fully labeled (red) and spin-diluted (black) endophilin 63R1 bound to membrane. Spin-dilution was accomplished by labeling with a mixture of R1 and its diamagnetic analogue R1' (4). Distance analysis was performed using analysis of the Pake pattern broadening function as implemented in the ShortDistances program generously provided by Drs. Altenbach and Hubbell. The fit obtained using the program is shown in blue and resulted in an inter-label distance of ~9Å. (D) As a control distance obtained for membrane-bound endophilin derivatives where compared to those obtained from soluble proteins. The baseline subtracted 4-pulse DEER data are shown in black, while the Gaussian fit is shown in red. The distance distribution corresponding to the observed oscillation is given in the right column.

Figure S2. Four-pulse DEER data obtained for membrane-bound endophilin derivatives. The baseline subtracted data are shown in black, while the Gaussian fit is shown in red. The distance distribution corresponding to the observed oscillation is also given.

Figure S3. Helices in the insert region are flexible. **A.** Motion of the A63-S75 helices in the SAMD calculation monitored using an angle (θ) between the helical axis and a line parallel to the long symmetry axis of the BAR domain. θ was defined as $C\alpha(74)-C\alpha(67)-C\alpha(182)$, where $C\alpha(74)-C\alpha(67)$ is an approximation of the helical axis and $C\alpha(182)$ was chosen such that θ was close to 90° when the A63-S75 helix was approximately orthogonal to the BAR domain axis. **B.** Representative structures for $\theta = 40^\circ$ (blue), 90° (green) and 140° (orange).

Figure S4. Interactions of hydrophobic residues in the helix insert (residues 63-75) in a conformation orthogonal to the BAR domain. L68 has stabilizing interactions with I55 and L58 of the BAR domain. I71 may interact with Y86 in the loop of the insert region.

Figure S5. Interactions of charged residues in the helix insert. Interactions of charged residues (R65 and K67) in the helix insert (residues 63-75) in conformations with $\theta = 40^\circ$ (blue), 140° (orange) and 90° (green) (see Fig. S4 for a definition of θ). The amino acids are labeled as “a” and “b” to denote the two subunits of the endophilin dimer. **A.** With the insert helices in the $\theta = 40^\circ$ conformation, R65a forms an intra-subunit salt bridge with E56a. A similar interaction occurs between R65b and E56b. **B.** In the $\theta = 140^\circ$ conformation, the insert helices are rotated such that K67a forms an inter-subunit

interaction with E56b. A similar interaction occurs between K67b and E56a. **C.** In the $\theta = 90^\circ$ conformation, neither R65 nor K67 have an interaction with E56.

Figure S1.

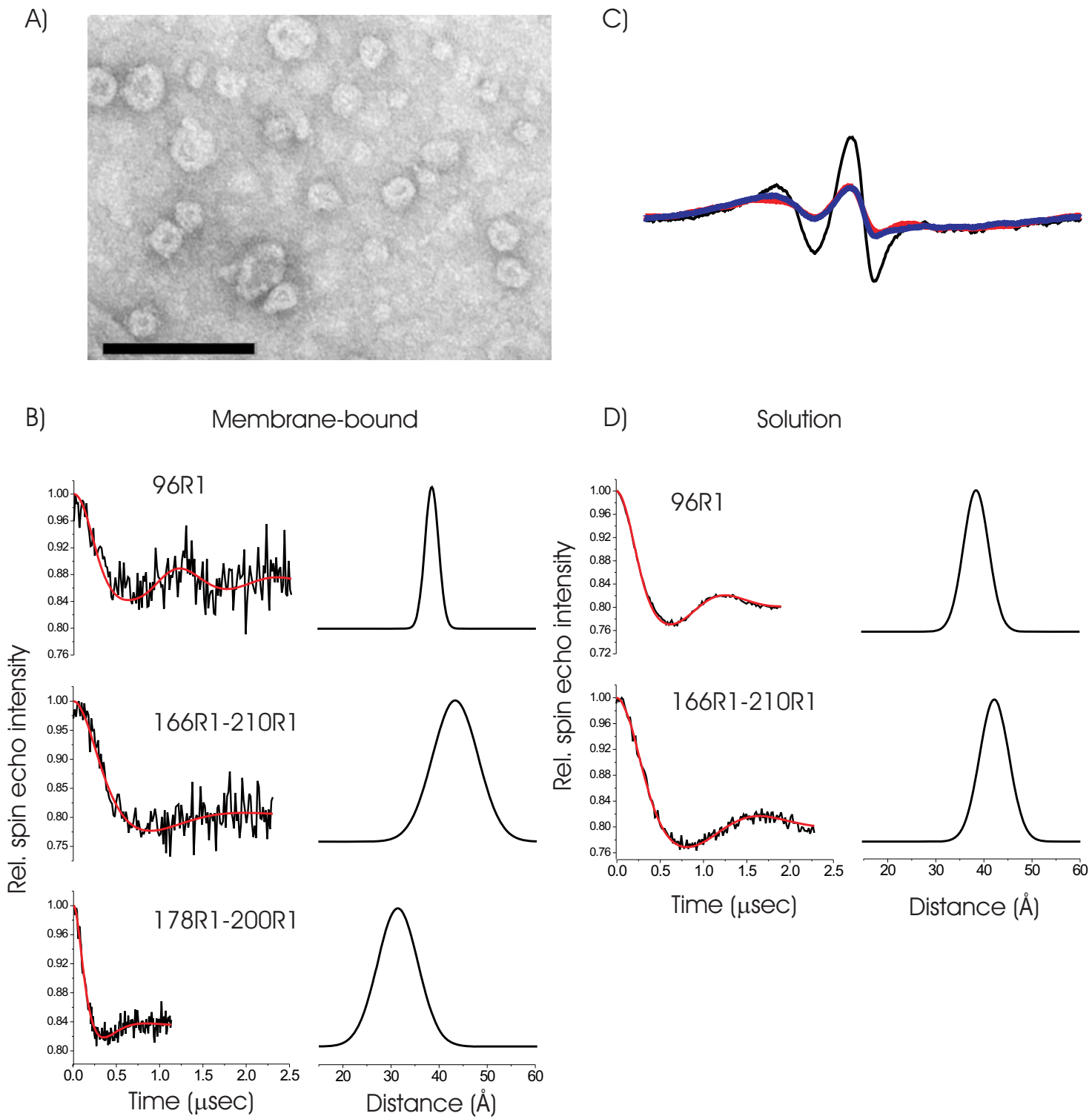


Figure S2.

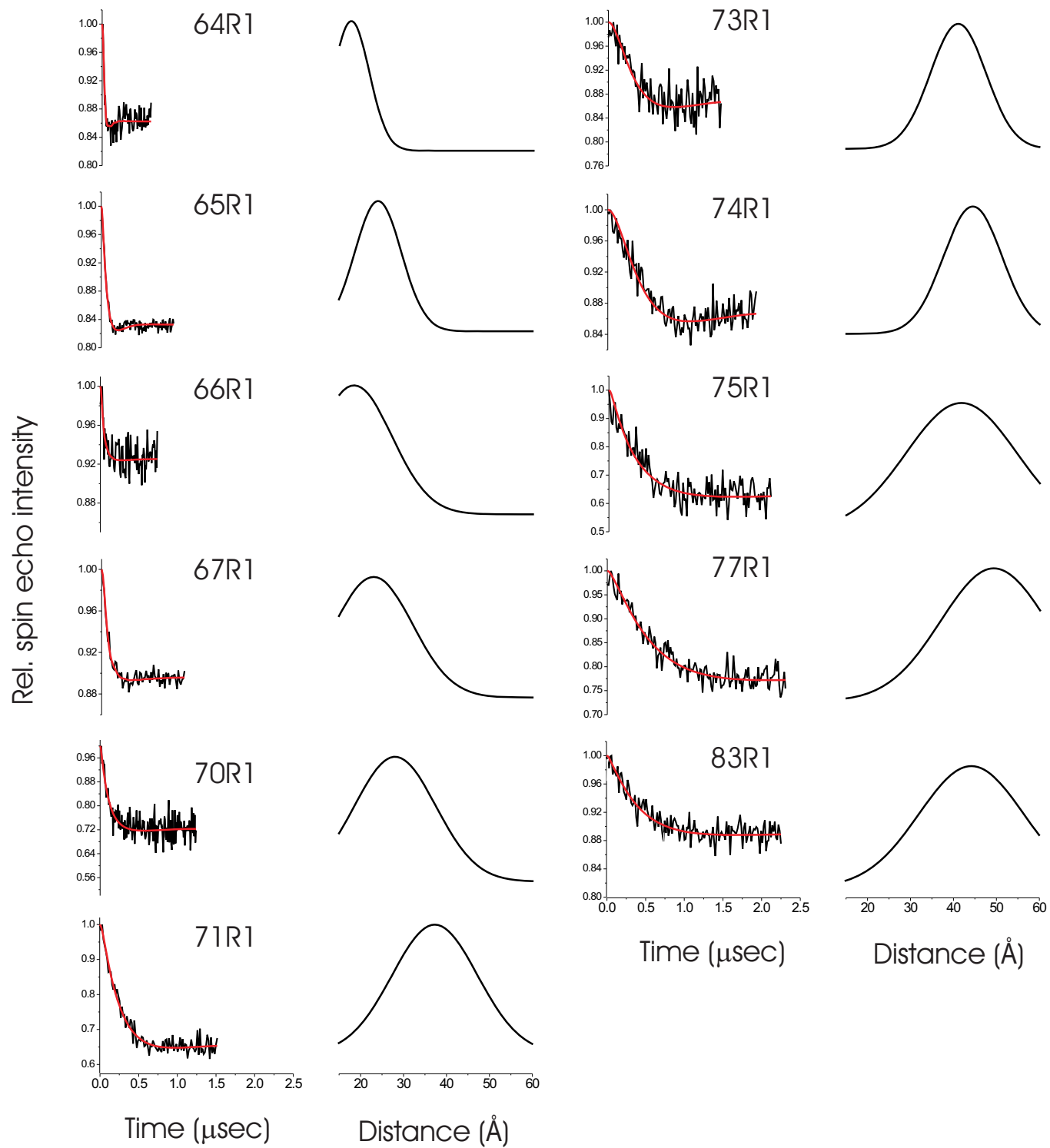
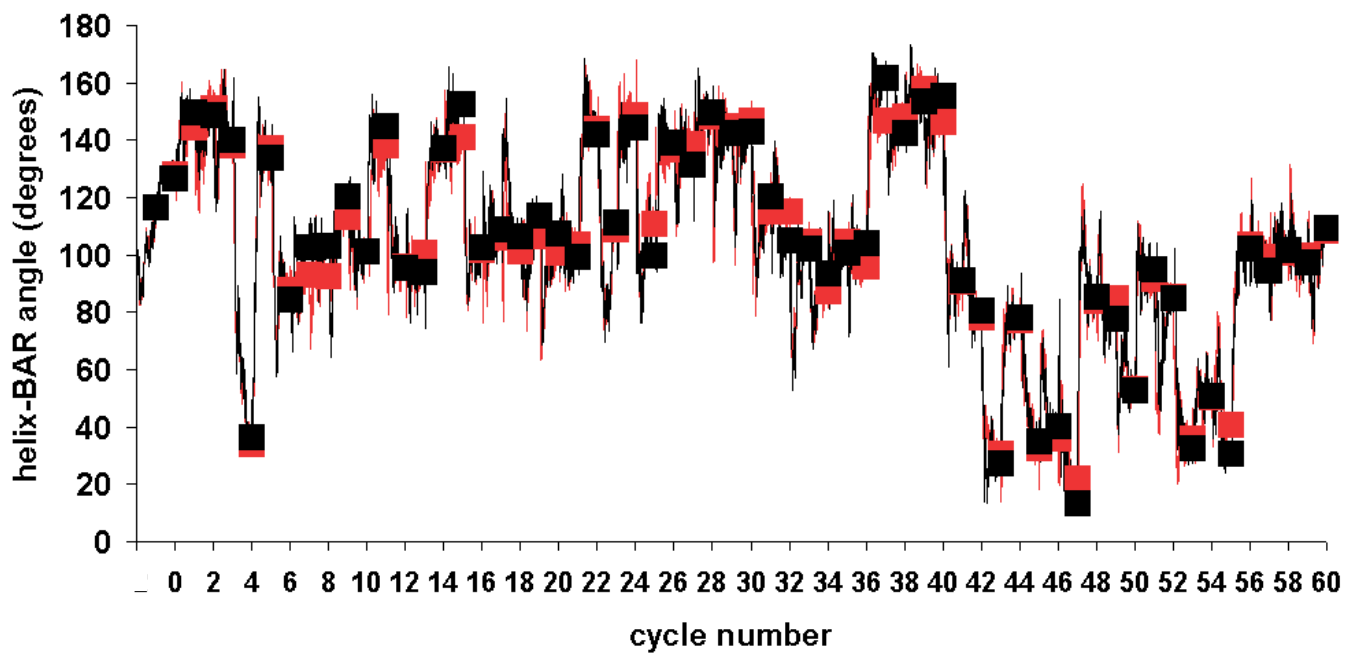


Figure S3.

A)



B)

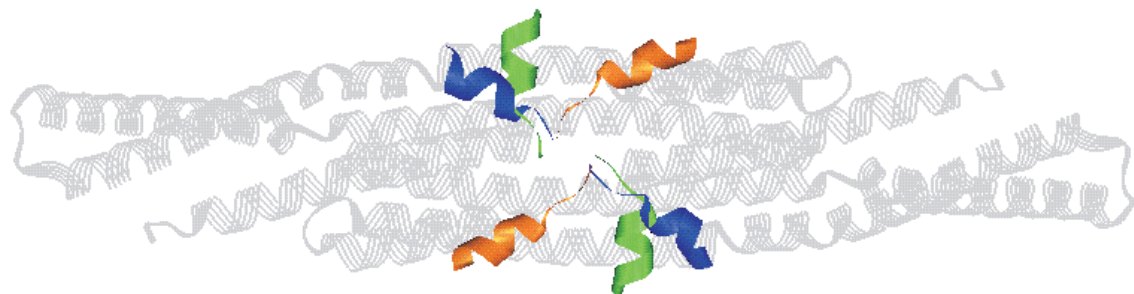


Figure S4.

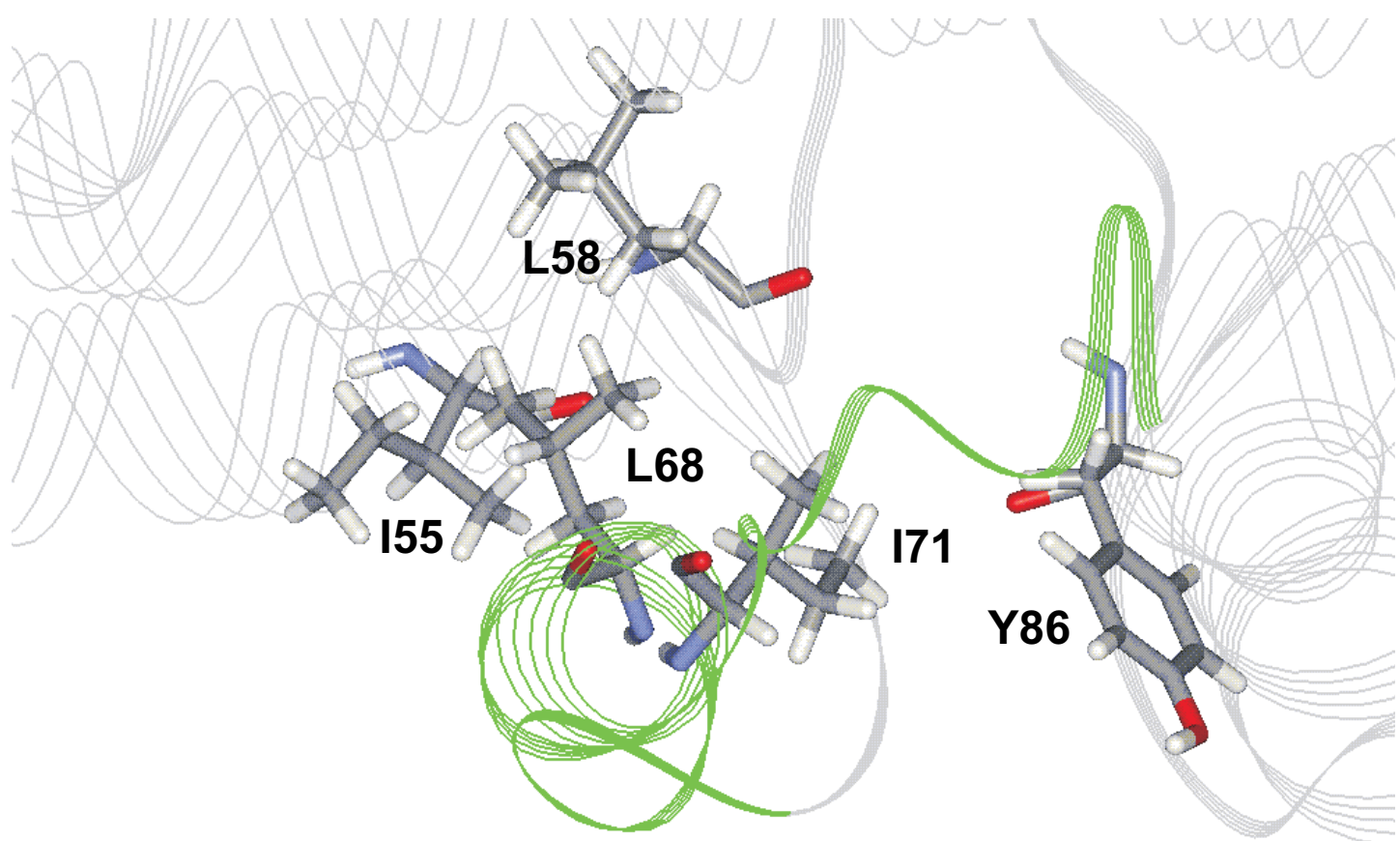


Figure S5.

Supplemental Material can be found at:
<http://www.jbc.org/content/suppl/2010/04/23/M110.127811.DC1.html>

